The Astrophysical Journal, 837:175 (9pp), 2017 March 10 https://doi.org/10.3847/1538-4357/aa62ff

Gamma–Gamma Absorption in the γ-ray Binary System PSR B1259-63/LS 2883

Iurii Sushch[1,2,3] and Brian van Soelen[4]
[1] Centre for Space Research, North-West University, 2520 Potcheftroom, South Africa; iurii.sushch@desy.de
[2] DESY, D-15738 Zeuthen, Germany
[3] Astronomical Observatory of Ivan Franko National University of L'viv, vul. Kyryla i Methodia, 8, 79005 L'viv, Ukraine
[4] Department of Physics, University of the Free State, 9300 Bloemfontein, South Africa; vansoelenb@ufs.ac.za
Received 2016 October 31; revised 2017 February 21; accepted 2017 February 22; published 2017 March 16

Abstract

The observed TeV light curve from the γ-ray binary PSR B1259-63/LS 2883 shows a decrease in the flux at periastron that has not been fully explained by emission mechanisms alone. This observed decrease can, however, be explained by $\gamma\gamma$ absorption due to the stellar and disk photons. We calculate the $\gamma\gamma$ absorption in PSR B1259-63/LS 2883 taking into account photons from both the circumstellar disk and star, assuming that the γ-rays originate at the position of the pulsar. The $\gamma\gamma$ absorption due to the circumstellar disk photons produces a $\approx$14% decrease in the flux, and there is a total decrease of $\approx$52% (>1 TeV) within a few days before periastron, accompanied by a hardening of the γ-ray photon index. While the $\gamma\gamma$ absorption alone is not sufficient to explain the full complexity of the H.E.S.S. γ-ray light curve, it results in a significant decrease in the predicted flux, which is coincident with the observed decrease. In addition, we have calculated an upper limit on the $\gamma\gamma$ absorption, assuming that the emission is produced at the apex of the bow shock. Future observations with CTA during the 2021 periastron passage may be able to confine the location of the emission based on the degree of $\gamma\gamma$ absorption, as well as measure the hardening of the spectrum around periastron.

Key words: gamma rays: stars – pulsars: individual (PSR B1259-63) – radiation mechanisms: non-thermal – stars: individual (LS 5039)

1. Introduction

The binary system PSR B1259-63/LS 2883 is a member of a small but growing class of sources known as γ-ray binaries, which at the moment comprises only six known objects. These systems consist of a compact object, believed to be either a pulsar or a black hole, in orbit around an early-type O or B star, and show a spectral energy distribution that peaks above 1 MeV (see Dubus 2013, for a detailed review of these systems). The most recently discovered system lies in the Large Magellanic Cloud, the first to be detected outside of the Milky Way (Corbet et al. 2016). This source has been detected at GeV energies by *Fermi*-LAT but, unlike for the other sources, TeV emission has not been reported. One other candidate γ-ray binary system, PSR J2032+4127/MT91 213, which contains a γ-ray pulsar, has also recently been highlighted by Ho et al. (2017). A possible TeV counterpart of this binary system, TeV J2032+4130, was one of the first sources ever detected at TeV energies and the first TeV source with no obvious counterpart at other wavelengths (Aharonian et al. 2002). The source, however, exhibits a steady TeV flux with no evidence of periodic behavior and was at first suggested to be the evolved pulsar wind nebula of PSR J2032+4127 (Aliu et al. 2014, and references therein). The recent discovery that the pulsar is in a ~30 yr orbit around MT91 213 and is expected to pass through periastron by the end of 2017 challenges the current interpretation (Ho et al. 2017; Lyne et al. 2015).

Unlike the other γ-ray binaries, where the nature of the compact object is unknown, in PSR B1259-63/LS 2883 it is known to be a 48 ms pulsar, which is in an eccentric ~3.4 yr orbit around the companion (Johnston et al. 1992a, 1992b; Shannon et al. 2014). For the other systems both pulsar and black hole scenarios have been widely discussed. The companion, LS 2883, is a Be star that is surrounded by a circumstellar disk, which is a region of enhanced stellar outflow (Johnston et al. 1992a, 1992b; Negueruela et al. 2011). Circumstellar disks around Be stars are known to generate infrared (IR) emission produced mainly through free–free radiation, which provides an additional target photon field for inverse Compton (IC) scattering (Khangulyan et al. 2012; van Soelen et al. 2012) and $\gamma\gamma$ absorption (Orellana & Romero 2007; Sushch & Böttcher 2014).

The disk is thought to be inclined with respect to the binary orbit, and the pulsar crosses it twice each orbit. The dense medium of the disk plays an important role in the resulting emission from the system. When the pulsar goes behind the disk, its pulsed radio emission disappears, at about $t_p - 20$ days, and it reappears again after the second crossing of the disk, at about $t_p + 15$ days, where t_p is the time of periastron. In this way the location of the disk is determined.

As the pulsar approaches periastron, there is an increase in the unpulsed nonthermal radio, X-ray, and TeV emission. The radio, X-ray, and TeV light curves show a similar behavior, exhibiting a double-peak structure (or a hint of a double-peak structure as in the case of the TeV light curve), with two asymmetrical peaks roughly coinciding with the time that the pulsar passes through the disk (see Chernyakova et al. 2014, and references therein). This suggests a possible connection between the equatorial disk and the variability of the nonthermal emission. The observed shape of the GeV light curve, however, strongly deviates from those at other wavebands, with only faint (if any) emission detected at periastron and a sudden and very powerful flare starting from approximately 30 days after periastron (Abdo et al. 2011; Tam et al. 2011, 2015; Caliandro et al. 2015; Chernyakova et al. 2015). This flare does not occur at the same time as the post-periastron peaks detected at other wavelengths (e.g., Chernyakova et al. 2015). The flare is now known to be

periodic as it has been detected around two consecutive periastron passages, though its cause is still not clear.

At TeV energies PSR B1259-63/LS 2883 has been observed by H.E.S.S. around four periastron passages, namely, 2004 (Aharonian et al. 2005), 2007 (Aharonian et al. 2009), 2010 (H.E.S.S. Collaboration et al. 2013), and 2014 (Romoli et al. 2015). The TeV emission shows a clear variable behavior around the periastron passage, with a suggestion of a double-peak structure, and a local minimum in the flux at periastron. The double-peak shape of the TeV light curve would suggest a hadronic scenario for the generation of the TeV emission. Indeed, if the pulsar wind is predominantly proton-loaded, one would expect two sharp peaks when the protons interact with the dense disk environment (Neronov & Chernyakova 2007). The hadronic scenario could also explain the radio and X-ray light curves as synchrotron and IC emission from the secondary electrons produced in the proton–proton interactions (Neronov & Chernyakova 2007). However, observations show that the TeV flux from the system begins to increase ∼50 days before periastron, before the pulsar reaches the location of the disk suggested by the radio eclipse, which makes the hadronic scenario rather unlikely. In the leptonic scenario one would expect the light curve either to peak close to periastron in the case of dominant adiabatic losses (due to the increased density of stellar photons and the most favorable scattering angle) or to show a smooth variability in the case of the saturation of the electron spectrum by radiation losses (Kirk et al. 1999). Neither of these predictions can explain the observed TeV light curve. In the case of the saturation regime, a weak variability of the TeV flux is expected, due to the orbital dependence of the scattering angle, which will result in the flux being slightly higher before periastron (compared to the flux after periastron), with a peak right before periastron, where the scattering angle is the largest. Kerschhaggl (2011) suggested that the introduction of time-dependent adiabatic losses, which are dominant over the whole orbit, could explain the observed TeV light curve. However, that study focused more on determining the profile of the time-dependent adiabatic cooling coefficient from the observational data, rather than explaining the physical reasons for such a profile.

The influence of the circumstellar disk on the nonthermal emission has also been investigated in smoothed particle hydrodynamics (SPH) simulations undertaken by Takata et al. (2012), which were able to roughly reproduce the X-ray light curve using a very dense disk ($\sim 10^{-9}$ g cm^{-3}; denser than typical). Here the pre- and post-periastron peaks in the X-ray and TeV light curves were interpreted as the pulsar spin-down power being converted to particle acceleration more efficiently when the pulsar passes through the disk. However, the model did not reproduce the GeV and TeV light curves (assuming IC emission) and predicted a peak in the flux around periastron, which is in contradiction with the observations.

The decrease in the TeV flux at periastron can be naturally explained by $\gamma\gamma$ absorption caused by stellar and disk photons. Indeed, the geometry of the system infers that $\gamma\gamma$ absorption would be most effective just before periastron since at that point the path of the emitted γ-ray photon toward the observer will pass at the closest distance to the star (and therefore through a higher density of photons) and at the most optimal interaction angle. Gamma–gamma absorption in γ-ray binaries, and in particular in PSR B1259-63/LS 2883, was thoroughly studied by Dubus (2006), who concluded that although $\gamma\gamma$ absorption should provide a significant effect on the observed TeV light curve from PSR B1259-63/LS 2883, this effect alone is not sufficient to explain the shape of the light curve. However, this study did not take into account the circumstellar disk of the Be star, which provides an additional photon field for $\gamma\gamma$ absorption. In addition to this, improved stellar parameters for LS 2883 have been obtained by Negueruela et al. (2011), which shows that the star has a higher effective temperature than previously thought. This in turn implies a higher photon energy density and hence stronger $\gamma\gamma$ absorption. Gamma–gamma absorption in the disk was briefly discussed in Sushch & Böttcher (2014), where it was shown that the disk might significantly contribute to the overall $\gamma\gamma$ absorption. However, Sushch & Böttcher (2014) used a simplified description of the disk and assumed that it had a constant width and a constant energy density. The maximum possible value for the energy density of the disk, for which the *Fermi*-LAT upper limits were not violated by the intrinsic flux and cascade emission, was used. For this value, the $\gamma\gamma$ absorption is stronger in the disk than in the stellar radiation field. Therefore, the calculated flux extinction in Sushch & Böttcher (2014) should only be considered as an upper limit for the stellar and binary parameters used in that work.

In this paper we revisit the problem of $\gamma\gamma$ absorption in PSR B1259-63/LS 2883 using a more realistic model of the circumstellar disk, with the energy density constrained by IR and optical observations of the star, and adopt the more updated stellar and binary parameters.

2. Astrophysical Properties of PSR B1259-63/LS 2883

2.1. Astrophysical Parameters

Long-term observations of the radio pulsar provide very accurate measurements of PSR B1259-63/LS 2883's orbital parameters. The pulsar (PSR B1259-63) is orbiting the Be star LS 2883 in a very eccentric orbit ($e = 0.87$) with an orbital period of 1236.72 days and a longitude of periastron of $\omega = 138\overset{\circ}{.}7$ (Johnston et al. 1992a, 1992b, 1994; Shannon et al. 2014). The binary system is at a distance of ≈2.3 kpc from Earth (Negueruela et al. 2011). The last periastron took place on 2014 May 4 (MJD 56,781.418307).

High-resolution optical spectroscopy of LS 2883 shows that the star rotates faster and is more luminous than was previously thought, and is oblate ($R_{\rm eq} \simeq 9.7\,R_\odot$ at the equator and $R_{\rm pole} \simeq 8.1\,R_\odot$ at the poles), with a temperature gradient from $T_{\rm eq} \simeq 27{,}500$ K to $T_{\rm pole} \simeq 34{,}000$ K (Negueruela et al. 2011). For a nonrotating star, the equivalent stellar parameters are $R_* = 9.2\,R_\odot$ and an effective temperature of $T_* = 33{,}500$ K (Negueruela et al. 2011). The mass of the star was estimated to be $M_* = 31\,M_\odot$; however, it is noted by the authors that the uncertainty in this could be large since it is dependent on the estimated distance to the source, as well as the corrections that must be applied as a result of stellar rotation (Negueruela et al. 2011).

Figure 1 illustrates a schematic picture of the binary system denoting the parameters that determine the complex geometry of the system and its spatial orientation. Assuming that the mass of the star is $M_* = 31\,M_\odot$ (with a radius $R_* = 9.2\,R_\odot$), the mass of the pulsar is $1.4\,M_\odot$, and the binary mass function is $f = 1.53\,M_\odot$ (Johnston et al. 1994), the orbital inclination angle of the system is $i = 22\overset{\circ}{.}2$, and at periastron the binary separation is $\simeq 21.9\,R_*$.

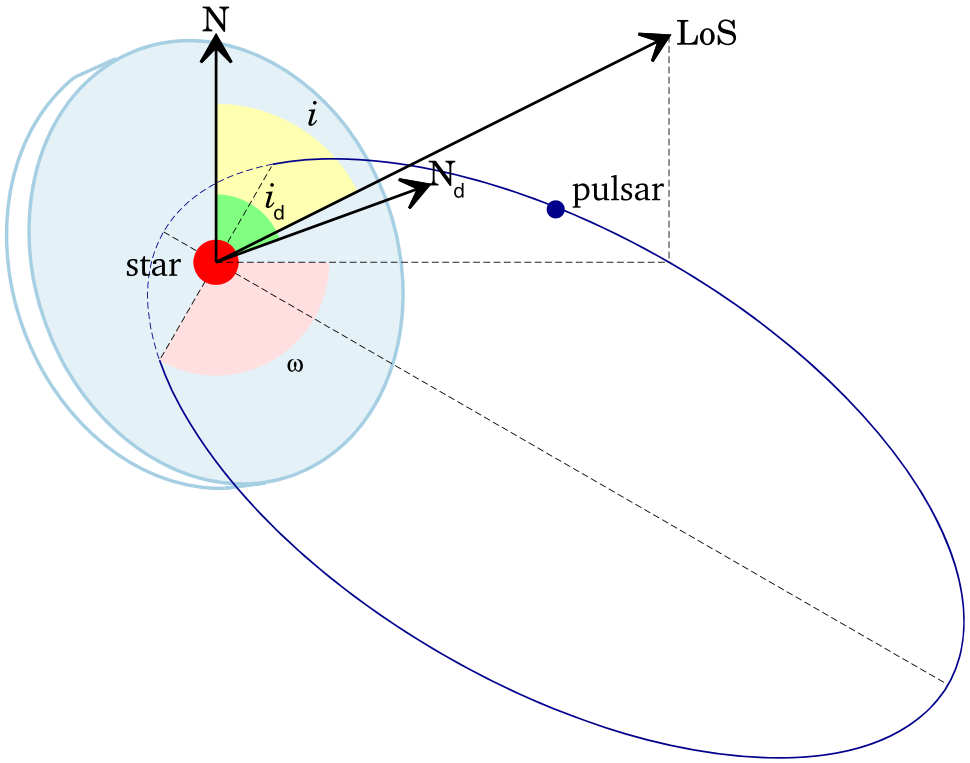

Figure 1. Schematic plot describing geometry of the binary system PSR B1259-63/LS 2883. N represents the normal to the orbital plane, and N_d is the normal to the plane of the disk. The inclination of the binary i, the inclination of the disk i_d, and the longitude of periastron ω are also shown. The pulsar is moving clockwise in this plot.

The inclination of the disk with respect to the orbit is argued to be small, approximately $i_d = 10^\circ$ or less (Melatos et al. 1995). The lower limit on the radius of the disk is $\sim 45\, R_*$, determined by the separation distance at $\sim$20 days from periastron. Hereafter the radius of the disk is assumed to be $R_{\rm disk} = 50\, R_*$. Circumstellar disks of Be stars are believed to be thin (see, e.g., Rivinius et al. 2013), and following other theoretical works on this system (e.g., Okazaki et al. 2011; Takata et al. 2012; van Soelen et al. 2012; Sushch & Böttcher 2014), we assume that the half-opening angle of the disk is $\theta_{\rm disk} = 1^\circ$ throughout the paper.

2.2. Radiation Field

The Be star LS 2883 produces the radiation field that provides the target photons for IC scattering and for $\gamma\gamma$ absorption of TeV γ-ray photons. The radiation field consists of two components, the stellar component from the star and a secondary component from the circumstellar disk.

The circumstellar disks of Be stars are known to produce IR radiation through free–free and free-bound scattering. We model the contribution from the disk following Waters (1986), where the disk is assumed to have a density profile given by

$$\rho(r) = \rho_0 \left(\frac{r}{R_*}\right)^{-n}, \tag{1}$$

where r is the distance from the center of the star, R_* is the radius of the star, and ρ_0 is the density at the base of the disk (at $r = R_*$). The density decreases with the profile index n. In this model it is assumed that the disk has a uniform temperature, $T_{\rm disk}$, a half-opening angle, $\theta_{\rm disk}$, and a maximum radius, $R_{\rm disk}$.

The emission from the disk is calculated from the optical depth due to free–free and free-bound scattering. It can be shown that the optical depth along a length, s, through the disk is given by (Lamers & Waters 1984; Waters 1986; van Soelen et al. 2012)

$$\tau_\nu = \int_0^{\bar{s}} d\bar{s}\; X_\lambda X_* \bar{r}^{-2n}, \tag{2}$$

where the barred distances are in units of stellar radii. Here,

$$X_\lambda = \lambda^2 [(1 - e^{-h\nu/kT_{\rm disk}})/(h\nu/kT_{\rm disk})] \times [g(\nu, T_{\rm disk}) + b(\nu, T_{\rm disk})] \tag{3}$$

contains the wavelength-dependent terms that vary with wavelength λ (and frequency ν), k is the Boltzmann constant, and $g(\nu, T_{\rm disk})$ and $b(\nu, T_{\rm disk})$ are the Gaunt factors for the free–free and free-bound scattering, respectively. The Gaunt factors are calculated following the approximation outlined in Waters & Lamers (1984), and for the analysis presented here we have only considered the contribution of the free–free scattering. The term X_* is given by

$$X_* = 4.923 \times 10^{35}\, \overline{z^2} T_{\rm disk}^{-3/2} \mu^{-2} \varpi \rho_0^2 \left(\frac{R_*}{R_\odot}\right), \tag{4}$$

where $\overline{z^2}$ is the mean of the squared atomic charge, μ is the mean atomic weight, and ϖ is the ratio of the number of electrons to the number of ions.

The parameters for the disk model are taken from the fit to the stellar and disk component used in van Soelen et al. (2012), which were fitted to near-IR and mid-IR observations of LS 2883. The parameters are summarized in Table 1.

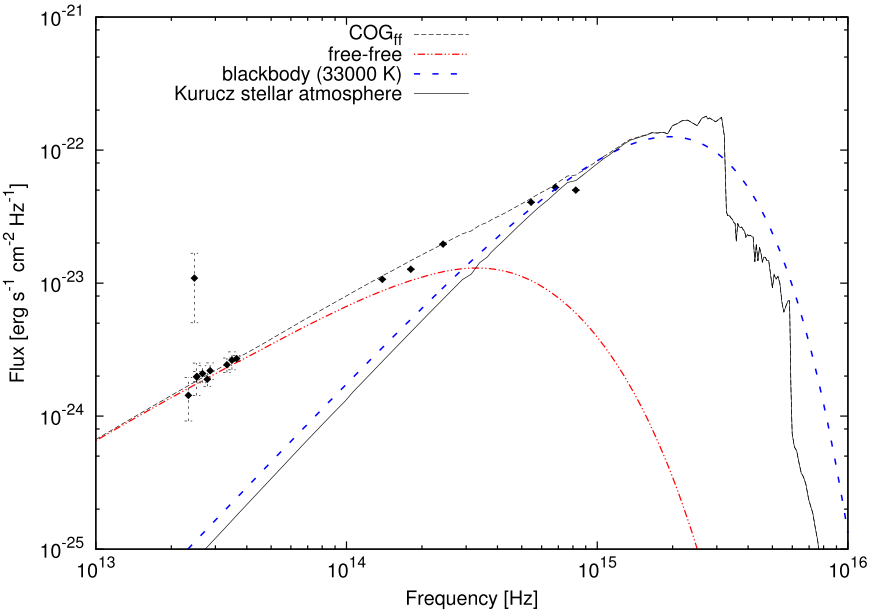

Figure 2. IR and optical observations from LS 2883 fitted with a stellar atmosphere (solid black line) and free-emission (red double-dot-dashed line), along with the combined contribution (black dashed line) as given in van Soelen et al. (2012). A 33,000 K blackbody distribution is plotted for comparison (blue dashed line).

Table 1
Parameters for the Disk Model

Parameter	Value
T_*	33,000 K
n	3.055
$\log_{10}X_*$	10.245
$R_{\rm disk}$	50 R_*
$T_{\rm disk}$	19,800 K
$\theta_{\rm disk}$	1°

Since, in this model, the disk is assumed to be in local thermodynamic equilibrium, the source function is given by the Planck function. The photon number density is therefore given by

$$n_{\rm disk}(\nu, \Omega) = \frac{I_\nu(\nu, \Omega)}{h\nu c} \quad (5)$$

$$= \frac{1}{h\nu c} B_\nu(T_{\rm disk})[1 - e^{-\tau_\nu}], \quad (6)$$

where h is the Planck constant, c is the speed of light, and $B_\nu(T_{\rm disk})$ is the Planck function.

The photon number density is calculated from Equation (6) in any direction by determining the optical depth in that direction due to the circumstellar disk. The optical depth is calculated by numerically integrating Equation (2) over $\bar{s}$, taking into account the geometry of the circumstellar disk. The code also determines whether any direction would intercept the star and correctly takes into account that regions of the disk are obscured and must not be included.

The contribution from the star has been modeled assuming that the star is a spherical blackbody emitter, with a temperature of 33,000 K and a radius of $R_* = 9.2\,R_\odot$ in order to be comparable to the previous model (van Soelen et al. 2012). Since the star is surrounded by the circumstellar disk, the disk will also attenuate emission from the star. Therefore, similarly to above, the number density from the star is calculated as

$$n_*(\nu, \Omega) = \frac{1}{h\nu c} B_\nu(T_*) e^{-\tau_\nu}, \quad (7)$$

where the stellar contribution is decreased by $\exp(-\tau_\nu)$ if it is observed through the disk. The model, compared to the observations, is shown in Figure 2.

3. Gamma–Gamma Absorption

Gamma-ray photons emitted in binary systems are subject to $\gamma\gamma$ absorption as they pass through the star's photon field (see, e.g., Dubus 2006). The interaction of a γ-ray photon with a low-energy photon can result in electron–positron pair production (Gould & Schréder 1967), if the energy exceeds the threshold condition for pair production, which is given by

$$\epsilon\epsilon_\gamma(1 - \cos\theta) \leqslant 2, \quad (8)$$

where ϵ and ϵ_γ denote the photon energies of the target low-energy photon and the γ-ray photon, respectively, normalized to the electron rest-mass energy, i.e., $\epsilon = h\nu/m_e c^2$, and θ is the interaction angle between the two photons. The minimum threshold occurs for a head-on collision ($\cos\theta = -1$), and for a 1 TeV gamma-ray photon this will require photons with a threshold frequency of

$$\nu \simeq 6.3 \times 10^{13} \left(\frac{h\nu_\gamma}{1\ {\rm TeV}}\right)^{-1} {\rm Hz}, \quad (9)$$

which is within the mid-IR regime (where the disk is the primary photon source; Figure 2).

The $\gamma\gamma$ optical depth is given by (Gould & Schréder 1967)

$$\tau_{\gamma\gamma} = \int_0^l dl \int_{4\pi} d\Omega\,(1 - \mu) \int_{\frac{2}{\epsilon_\gamma(1-\mu)}}^{\infty} d\epsilon\; n_{\rm ph}(\epsilon, \Omega)\sigma_{\gamma\gamma}(\epsilon, \epsilon_\gamma, \mu), \quad (10)$$

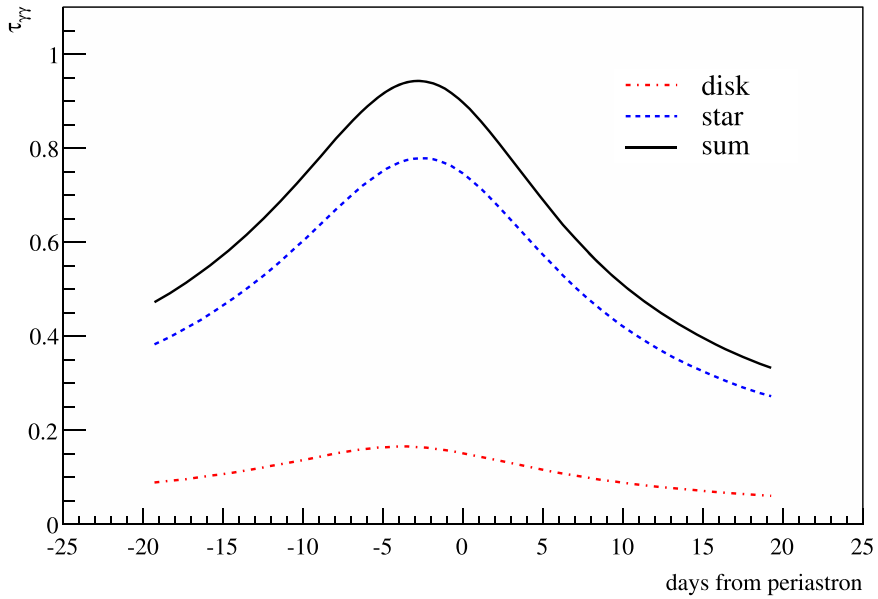

Figure 3. The $\gamma\gamma$ optical depth of the Be star's radiation field as a function of time around periastron for a 1 TeV γ-ray photon. The blue dashed line denotes the stellar component, the red dot-dashed line denotes the circumstellar disk component, and the combined effect is shown by the solid black line.

where l is the distance over which the γ-ray photon travels, $\mu = \cos\theta$, $d\Omega = d\mu d\phi$, and $n_{\rm ph}(\epsilon, \Omega)$ is the number density of the low-energy target photons. Here, $\sigma_{\gamma\gamma}$ is the $\gamma\gamma$ cross section (Jauch & Rohrlich 1976),

$$\sigma_{\gamma\gamma}(\beta) = \frac{3}{16}\sigma_{\rm T}(1-\beta^2) \times\left[(3-\beta^4)\ln\left(\frac{1+\beta}{1-\beta}\right) - 2\beta(2-\beta^2)\right], \quad (11)$$

where

$$\beta = \sqrt{1 - \frac{2}{\epsilon\epsilon_\gamma(1-\mu)}}, \quad (12)$$

and $\sigma_{\rm T}$ is the Thomson cross section. The maximum $\gamma\gamma$ cross section occurs when the energy of the interacting photons is twice that of the energy threshold (Equation (8)). This implies that for TeV γ-ray photons the $\gamma\gamma$ interaction is a maximum for IR photons at a frequency

$$\nu \simeq 1.3\times 10^{14}\left(\frac{h\nu_\gamma}{1\ {\rm TeV}}\right)^{-1}\ {\rm Hz}. \quad (13)$$

We treat the two components of the target radiation field (stellar radiation and circumstellar disk radiation) separately and numerically calculate the $\gamma\gamma$ optical depth of both components for a γ-ray photon traveling in the direction of the observer. The total optical depth is given by the sum of the optical depths of the two components. Figure 3 shows the optical depth for a γ-ray photon with an energy of 1 TeV as a function of time from periastron. As expected, the $\gamma\gamma$ optical depth due to the photons from the disk is lower than that due to the star but still results in a ≈15% decrease of the flux at TeV energies. The total decrease of the flux at 1 TeV due to $\gamma\gamma$ absorption may reach ∼60%. For the geometrical configuration used in our calculations (see Section 2.1) the maximum absorption due to the disk is at ≈4 days prior to periastron and that due to the star is at ≈2 days before periastron.

4. TeV Emission

We assume that the TeV emission from PSR B1259-63/LS 2883 is produced by relativistic particles accelerated at the termination shock that occurs between the pulsar and stellar winds. The location of the termination shock depends on the ratio of the pulsar to stellar wind power and on the binary separation distance. Moreover, the mass-loss rate and velocity of the stellar wind are different in the equatorial and polar regions. Therefore, the location and morphology of the shock change across the orbit. However, close to periastron, given that the inclination angle of the disk is rather small ($i_d \sim 10°$), the environment around the pulsar is strongly influenced by the dense equatorial disk, and the termination shock should form close to the pulsar (see discussion in Sushch & Böttcher 2014). Therefore, we assume the source of the TeV emission to be point-like and neglect the distance between the pulsar and the termination shock. In Section 5, we will briefly discuss how our results depend on the location of the termination shock.

In order to determine how the TeV observations will be affected by the $\gamma\gamma$ absorption, we have modeled the TeV light curve around periastron assuming an intrinsic power-law photon distribution,

$$\frac{dN}{dE} = N_0\left(\frac{E}{1\ {\rm TeV}}\right)^{-\Gamma}, \quad (14)$$

with a photon index of $\Gamma = 3.0$. For the region around periastron we assume a constant flux and that the variation is only due to the change in $\gamma\gamma$ absorption. In Figure 4 the results are compared to the gamma-ray flux detected by H.E.S.S. (>1 TeV) normalized to the highest flux value.

The $\gamma\gamma$ absorption from the disk photons alone results in a decrease of ≈14%, which is a maximum at ≈4 days before periastron. Similarly, including the stellar contribution results in a maximum total absorption of ≈52% at ≈2 days before periastron. This is comparable to the results calculated for a 1 TeV photon.

The energy dependence of the $\gamma\gamma$ absorption also results in a variation of the photon index around periastron. We determine

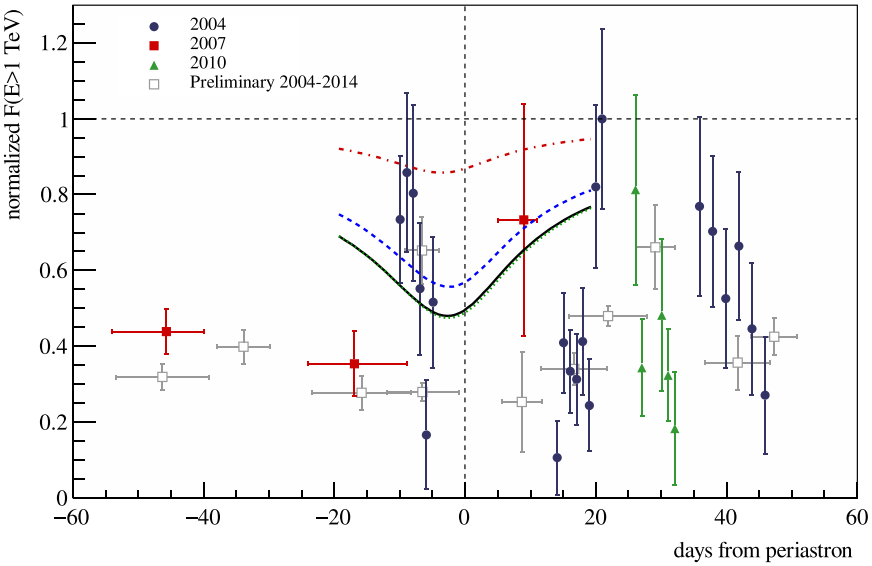

Figure 4. Flux (>1 TeV) around periastron assuming that the underlying intrinsic flux is constant, with a photon index $\Gamma = 3.0$. The plot shows the absorption due to disk photons (red dot-dashed line), the stellar photons (blue dashed line), and the combined effect (solid black line). The H.E.S.S. data (colored, filled symbols) are from H.E.S.S. Collaboration et al. (2013), while the open squares show the preliminary data reported by Romoli et al. (2015). The dotted green line shows the $\gamma\gamma$ absorption due to the stellar photons if the emission is produced at the apex of bow shock as discussed in Section 5.

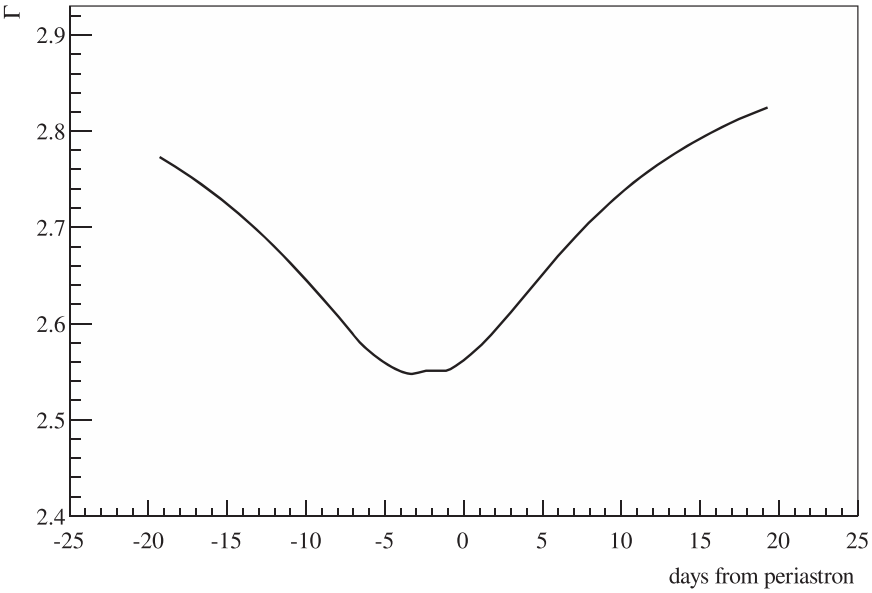

Figure 5. Variation in the gamma-ray photon index in the energy range 1–50 TeV around periastron due to $\gamma\gamma$ absorption assuming an intrinsic photon index of $\Gamma = 3.0$.

how the TeV γ-ray photon index changes by calculating the $\gamma\gamma$ absorption for an intrinsic power-law photon distribution ($\Gamma = 3.0$) and find the best-fit power-law distribution for the absorbed spectrum in the 1–50 TeV energy range. Figure 5 shows the photon index variability around periastron. The photon index varies between $\sim$2.6 and 2.8, becoming harder near periastron. This result is comparable to the photon index ($\Gamma \approx 2.8$) measured by H.E.S.S. away from periastron.

5. Discussion

5.1. TeV Light Curve

The results of the $\gamma\gamma$ absorption, taking into account both the disk and stellar component (with the updated stellar parameters), show that it will have a significant effect on the observed TeV light curve. Gamma–gamma absorption causes a significant decrease in the flux within a few days from periastron, which is coincident with a dip in the observed flux. Note that the observed flux shown in Figure 4 is normalized to the highest flux data point, which reflects the daily averaged flux $\sim$20 days after the 2004 periastron. Preliminary results of the reanalysis of all the H.E.S.S. data (Romoli et al. 2015) show period-averaged fluxes with absolute values somewhat lower (but still compatible within errors) than the daily averaged fluxes from the 2004 periastron (Figure 4). Compared to the reanalyzed data only (gray open squares in Figure 4), the modeled light curve can reproduce not only the location of the dip but also its depth. However, $\gamma\gamma$ absorption alone is not sufficient to explain the full complexity of the observed TeV light curve around periastron. For example, the steep decrease

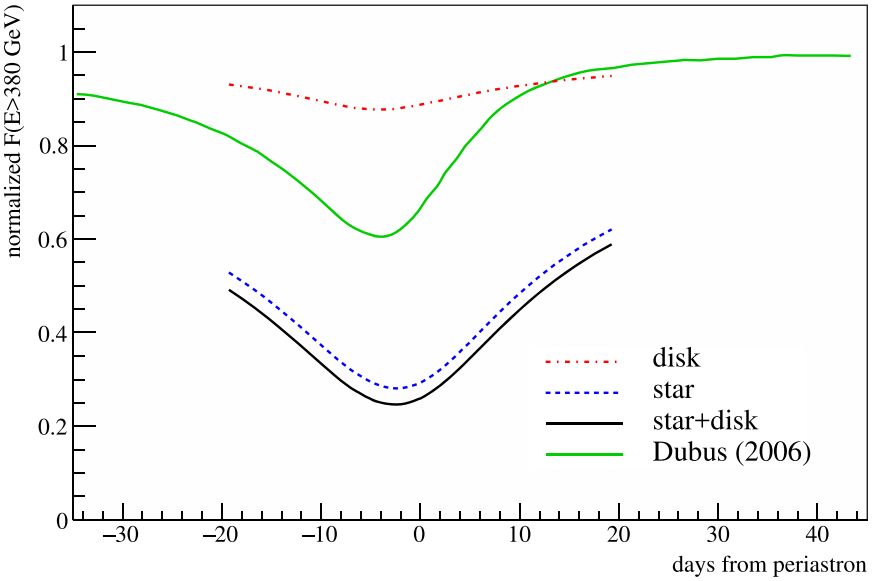

Figure 6. Integrated $\gamma\gamma$ absorption above 380 GeV due to the photons from the star and circumstellar disk assuming a power-law photon distribution with $\Gamma = 2.8$. The green solid line shows the $\gamma\gamma$ absorption found in Dubus (2006) compared to the updated emission as found here for the disk (dot-dashed red line) and star (dashed blue line). The solid black line shows the combined contribution.

of the observed flux before periastron is not compatible with the rather smooth decrease predicted by $\gamma\gamma$ absorption. Therefore, some variable features must be present already in the intrinsic flux from the source. In this study we do not model the emission from the source, nor do we consider the complicated morphology of the termination shock (see below), which might further modify the TeV light curve. Instead, we assume that the intrinsic TeV emission is constant close to periastron and that the emitting region is point-like, in order to isolate the effect of the $\gamma\gamma$ absorption and its impact on the resulting light curve.

The effect of the $\gamma\gamma$ absorption is larger than was found using the previous stellar parameters (Dubus 2006), and the minimum in the light curve is also shifted slightly owing to the updated orbital parameters. The increase in the absorption due to the updated stellar parameters is more apparent at lower energies. Figure 6 shows the integrated $\gamma\gamma$ absorption above 380 GeV, assuming an intrinsic photon index of $\Gamma = 2.8$, in order to make a more direct comparison to the results by Dubus (2006). The combined star and disk contribution leads to a maximum integrated $\gamma\gamma$ absorption of $\sim$75%.

The disk contribution to the overall $\gamma\gamma$ absorption is much smaller than was suggested in Sushch & Böttcher (2014). This is, however, not surprising, as in that work the $\gamma\gamma$ absorption in the disk was calculated for the highest possible disk energy density for which the *Fermi*-LAT upper limits were not violated, while in this work the disk radiation field is constrained by IR observations of the star. The different shape of the orbital-dependent $\gamma\gamma$ absorption is due to the more realistic description of the disk presented in this work compared to the simplified assumptions of constant width and density applied in Sushch & Böttcher (2014).

While our model has accurately taken into account the full geometric effect of the star and the circumstellar disk, for simplicity the emitting region has been considered as a point source located at the position of the pulsar. However, hydrodynamic simulations of colliding stellar and pulsar winds in binary systems show that the orbital evolution of the wind interaction results in a very complicated shock morphology with strongly entangled features (see Bosch-Ramon et al. 2015, and references therein). It is unclear where relativistic particles and, subsequently, γ-ray emission are produced. If the TeV emission is produced far from the apex of the shock, $\gamma\gamma$ absorption might be negligible since the path of the emitted γ-ray photon will lie far from the star and the radiation density will be much lower. Contrary to this, if the TeV emission is produced near the apex of the shock, TeV photons will pass closer to the star and the higher optical energy density will result in a larger $\gamma\gamma$ optical depth. The distance from the pulsar to the apex of the shock is given by (Eichler & Usov 1993)

$$r_{\rm p} = d\frac{\sqrt{\eta}}{(1+\sqrt{\eta})}, \tag{15}$$

where d is the distance between the pulsar and the star and η is the winds' ram pressure ratio, which is estimated to be $\eta = (0.03\text{–}0.08)$ for the polar wind (see Sushch & Böttcher 2014, and references therein). In this case the maximum distance from the pulsar to the apex of the shock is $r_{\rm p} = 0.22d$. The green dotted curve in Figure 4 shows the absorption above 1 TeV due only to the stellar (and not the disk) photons under the assumption that the TeV emission is produced at the apex of the shock and that the distance to the apex is a constant fraction of the separation distance, $r_{\rm p} = 0.22d$. This can be considered as an upper limit for the $\gamma\gamma$ absorption in the system. The absorption is similar to that found by the more detailed analysis, which also considered the $\gamma\gamma$ absorption due to the disk, but assumed that the emission originated at the position of the pulsar. Future observations with the much more sensitive CTA (Actis et al. 2011), combined with the predicted extinction of flux due to $\gamma\gamma$ absorption, might provide a hint of the location of the TeV γ-ray emission in the system.

5.2. Spectral Energy Distribution

In order to investigate how $\gamma\gamma$ absorption will affect the observed γ-ray spectral energy distribution, we have calculated

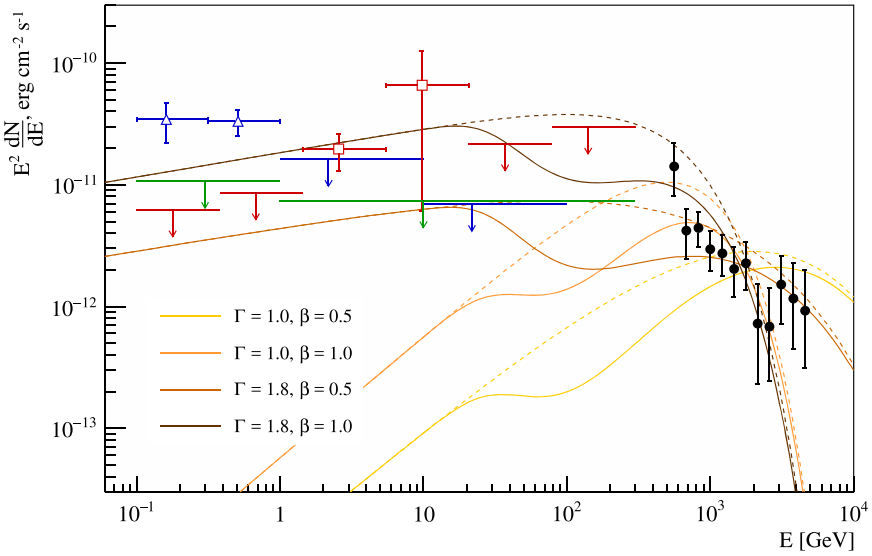

Figure 7. Spectral energy distribution of PSR B1259-63/LS 2883 with the associated photon distributions discussed in the text. The *Fermi*-LAT results from the 2010 periastron are taken from Abdo et al. (2011; blue triangles) and from Tam et al. (2011; red squares), and those from the 2014 periastron are taken from Tam et al. (2015; green upper limits). The H.E.S.S. data are from the 2010 periastron (H.E.S.S. Collaboration et al. 2013). The intrinsic (dashed lines) and $\gamma\gamma$ absorbed (solid lines) photon spectra are plotted for different parameters.

the absorbed $\sim$0.1–10^4 GeV spectrum assuming that the underlying photon spectrum is given by a power law with a super-exponential cutoff,

$$\frac{dN}{dE} = N_0 \left(\frac{E}{1\ \mathrm{TeV}}\right)^{-\Gamma} \exp\left[-\left(\frac{E}{E_c}\right)^{\beta}\right], \qquad (16)$$

which is a typical distribution for γ rays produced via IC scattering. Since the numerical calculation of the contribution from the disk is very computationally expensive and the $\gamma\gamma$ absorption is dominated by the stellar photons (particularly below 1 TeV), we have calculated the $\gamma\gamma$ absorption at periastron, only considering the stellar contribution. The model is compared to the TeV observations $\sim$30 days after periastron, which is comparable to the average flux detected around periastron, and is normalized assuming a flux of $F(>1\ \mathrm{TeV}) = 1.01 \times 10^{-12}\ \mathrm{cm}^{-2}\ \mathrm{s}^{-1}$ (H.E.S.S. Collaboration et al. 2013). The photon spectra for $\Gamma = 1.0$ and 1.8 and for $\beta = 0.5$ and 1.0, with a constant cutoff energy of $E_c = 500$ GeV, are shown in Figure 7.[5] The $\gamma\gamma$ absorption results in a decrease around 100 GeV, which makes it easier to reconcile the H.E.S.S. observations with the *Fermi*-LAT observations close to periastron. While pair cascading may slightly increase the emission in the GeV range, the effect will be too low to change these results (Sushch & Böttcher 2014).

5.3. Variation in Photon Index

As discussed above, the variation in the photon index (Figure 5) is compatible with observations away from periastron. However, the sensitivity of the current H.E.S.S. array is too low to detect the predicted variation at periastron. If this model is correct, there will be a hardening of the spectrum as the pulsar reaches periastron. Since the source is currently detectable with H.E.S.S., the improved sensitivity of CTA (Actis et al. 2011) will allow for a better detection of the system around periastron and may allow for this change in photon index to be measurable. While observations are not possible during the following periastron (2017 September), they will be possible during the next, in 2021 February, when conditions will be far more favorable for attempting to observe this effect.

[5] Please note that this choice of Γ is chosen to correspond to the spectrum of the broad γ-ray range and is different from the photon spectrum only in the *Fermi* or H.E.S.S. energy range. This range of values for the photon index Γ was considered to accommodate $\Gamma = 1.5$, which corresponds to the canonical value of the shock-accelerated particle spectrum index of 2.0.

6. Summary

The binary system PSR B1259-63/LS 2883 is part of the growing class of γ-ray binaries. The production of TeV γ-rays in this system is most commonly assumed to be produced through the acceleration of electrons in the shock that forms between the pulsar and stellar winds and the subsequent cooling of these electrons through IC scattering. These high-energy photons exceed the threshold for pair production, which should lead to a decrease in the TeV regime through $\gamma\gamma$ absorption.

Gamma–gamma absorption was previously investigated for the known systems by Dubus (2006); however, since then further observations have refined the binary and stellar parameters. We have reinvestigated $\gamma\gamma$ absorption in PSR B1259-63/LS 2883 incorporating the newer stellar and binary parameters (e.g., Negueruela et al. 2011; Shannon et al. 2014), as well as taking into account the contribution from the circumstellar disk.

We have shown that the combined contribution of the circumstellar disk and star results in an extinction of $\sim$52% of the very high energy γ-rays (>1 TeV) a few days before periastron. This maximum in the absorption is consistent with the dip in the flux observed by the H.E.S.S. telescope array; therefore, we suggest that $\gamma\gamma$ absorption is a major contributing factor to the TeV light curve and also contributes to the nondetection of the source in the $\sim$100 GeV energy range. The $\gamma\gamma$ absorption will produce a hardening of the TeV spectrum around periastron, an effect that may be observable with CTA around the 2021 periastron passage.

Lastly, the exact location of the production of the γ rays in γ-ray binaries is still unclear. We have in addition calculated an upper limit to the $\gamma\gamma$ absorption (due to the stellar photons alone) by also calculating the absorption if the γ-rays are produced at the apex of the bow shock assuming $r_{\rm p} = 0.22d$. This results in a maximum extinction of $\sim$50% of the flux above 1 TeV. The additional contribution of the disk to the total absorption would be $\gtrsim$14%, suggesting that the maximum absorption could be $\gtrsim$65% if the circumstellar disk is included. More sensitive observations with CTA may provide constraints on the magnitude of the $\gamma\gamma$ absorption in this system, which, combined with these estimates, might hint at the location of the TeV γ-ray emission in this system and the other γ-ray binaries.

This work was supported by the Department of Science and Technology and the National Research Foundation of South Africa through a block grant to the South African Gamma-Ray Astronomy Consortium. The numerical calculations were performed using the University of the Free State High Performance Computing Unit. The authors thank Maxim Barkov for fruitful discussions.

References

Abdo, A. A., Ackermann, M., Ajello, M., et al. 2011, ApJL, 736, L11
Actis, M., Agnetta, G., Aharonian, F., et al. 2011, ExA, 32, 193
Aharonian, F., Akhperjanian, A., Beilicke, M., et al. 2002, A&A, 393, L37
Aharonian, F., Akhperjanian, A. G., Anton, G., et al. 2009, A&A, 507, 389
Aharonian, F., Akhperjanian, A. G., Aye, K.-M., et al. 2005, A&A, 442, 1
Aliu, E., Aune, T., Behera, B., et al. 2014, ApJ, 783, 16
Bosch-Ramon, V., Barkov, M. V., & Perucho, M. 2015, A&A, 577, A89
Caliandro, G. A., Cheung, C. C., Li, J., et al. 2015, ApJ, 811, 68
Chernyakova, M., Abdo, A. A., Neronov, A., et al. 2014, MNRAS, 439, 432
Chernyakova, M., Neronov, A., van Soelen, B., et al. 2015, MNRAS, 454, 1358
Corbet, R. H. D., Chomiuk, L., Coe, M. J., et al. 2016, ApJ, 829, 105
Dubus, G. 2006, A&A, 451, 9
Dubus, G. 2013, A&ARv, 21, 64
Eichler, D., & Usov, V. 1993, ApJ, 402, 271
Gould, R. J., & Schréder, G. P. 1967, PhRv, 155, 1404
H.E.S.S. Collaboration, Abramowski, A., Acero, F., et al. 2013, A&A, 551, A94
Ho, W. C. G., Ng, C.-Y., Lyne, A. G., et al. 2017, MNRAS, 464, 1211
Jauch, J. M., & Rohrlich, F. 1976, Texts and Monographs in Physics (2nd ed.; New York: Springer)
Johnston, S., Lyne, A. G., Manchester, R. N., et al. 1992a, MNRAS, 255, 401
Johnston, S., Manchester, R. N., Lyne, A. G., et al. 1992b, ApJL, 387, L37
Johnston, S., Manchester, R. N., Lyne, A. G., Nicastro, L., & Spyromilio, J. 1994, MNRAS, 268, 430
Kerschhaggl, M. 2011, A&A, 525, A80
Khangulyan, D., Aharonian, F. A., Bogovalov, S. V., & Ribó, M. 2012, ApJL, 752, L17
Kirk, J. G., Ball, L., & Skjæraasen, O. 1999, APh, 10, 31
Lamers, H. J. G. L. M., & Waters, L. B. F. M. 1984, A&A, 136, 37
Lyne, A. G., Stappers, B. W., Keith, M. J., et al. 2015, MNRAS, 451, 581
Melatos, A., Johnston, S., & Melrose, D. B. 1995, MNRAS, 275, 381
Negueruela, I., Ribó, M., Herrero, A., et al. 2011, ApJL, 732, L11
Neronov, A., & Chernyakova, M. 2007, Ap&SS, 309, 253
Okazaki, A. T., Nagataki, S., Naito, T., et al. 2011, PASJ, 63, 893
Orellana, M., & Romero, G. E. 2007, Ap&SS, 309, 333
Rivinius, T., Carciofi, A. C., & Martayan, C. 2013, A&ARv, 21, 69
Romoli, C., Bordas, P., Mariaud, C., et al. 2015, arXiv:1509.03090
Shannon, R. M., Johnston, S., & Manchester, R. N. 2014, MNRAS, 437, 3255
Sushch, I., & Böttcher, M. 2014, JHEAp, 3, 18
Takata, J., Okazaki, A. T., Nagataki, S., et al. 2012, ApJ, 750, 70
Tam, P. H. T., Huang, R. H. H., Takata, J., et al. 2011, ApJL, 736, L10
Tam, P. H. T., Li, K. L., Takata, J., et al. 2015, ApJL, 798, L26
van Soelen, B., Meintjes, P. J., Odendaal, A., & Townsend, L. J. 2012, MNRAS, 426, 3135
Waters, L. B. F. M. 1986, A&A, 162, 121
Waters, L. B. F. M., & Lamers, H. J. G. L. M. 1984, A&AS, 57, 327